Inorg. Chem. **2008**, *47*, 6245−6253

Wheel-Shaped Mn_{16} Single-Molecule Magnets

Sonali J. Shah,[†] Christopher M. Ramsey,[§] Katie J. Heroux,[†] James R. O'Brien,[‡] Antonio G. DiPasquale,[†] Arnold L. Rheingold,[†] Enrique del Barco,[§] and David N. Hendrickson*[,†]

Department of Chemistry and Biochemistry, University of California at San Diego, La Jolla, California 92093, Quantum Design, San Diego, California 92121, and Department of Physics, University of Central Florida, Orlando, Florida 32765

Received February 12, 2008

The syntheses, structures, and magnetic properties of two new single-stranded hexadecanuclear manganese wheels $[Mn_{16}(CH_3COO)_8(CH_3CH_2CH_2COO)_8(teaH)_{12}]\cdot 10$ MeCN (**1**·10 MeCN) and $[Mn_{16}((CH_3)_2CHCOO)_{16}(teaH)_{12}]\cdot 4CHCl_3$ (**2**·$4CHCl_3$), where $teaH^{2-}$ is the dianion of triethanolamine, are reported. **1** crystallizes in the tetragonal $I4_1/a$ space group [$a = b = 33.519(4)$ Å and $c = 16.659(2)$ Å]. **2** crystallizes in the monoclinic $C2/c$ space group [$a = 21.473(5)$, $b = 26.819(6)$, $c = 35.186(7)$, and $\beta = 93.447(5)°$]. Both complexes consist of 8 Mn(II) and 8 Mn(III) ions alternating in a wheel-shaped topology with 12 monoprotonated triethanolamine ligands. Variable-temperature direct current (DC) magnetic susceptibility data were collected in 1 T, 0.1 and 0.01 T fields, and in the 1.8−300 K temperature range for **1** and **2**. Variable-temperature variable-field DC magnetic susceptibility data were obtained in the 1.8−10 K and 0.1−5 T ranges and least-squares fitting of these reduced magnetization versus H/T data indicates a $S = 13$ ground-state for **1** and **2**. Single-crystal magnetization hysteresis measurements were performed in a 0.04−1 K temperature range for complex **2**. Hysteresis loops were observed that showed a temperature dependence, which indicates that **2** exhibits magnetization relaxation and is a SMM. Both **1** and **2** show frequency-dependent out-of-phase signals in the AC susceptibility measurements, collected in a temperature range of 1.8−5 K and in the frequency range of 50−10 000 Hz. Extrapolation of the in-phase component of the AC susceptibility data to 0 K indicates an $S = 12$ ground state for **1** and an $S = 11$ ground-state for **2**. Complex **1** has the highest-spin ground state reported to date for a single-stranded manganese wheel and is likely to be an SMM based on a frequency-dependent out-of-phase signal in the AC susceptibility. The AC susceptibility as well as magnetization hysteresis data for **2** confirm that this species is an SMM.

Introduction

Single-molecule magnets (SMMs) have attracted much attention in recent years. SMMs are polynuclear metal complexes that have a large spin (S) ground state, with a negative axial zero-field splitting parameter D that leads to an appreciable potential energy barrier for magnetization reversal. SMMs are found to show magnetization relaxation, a property of classical magnets, as well as quantum effects such as quantum tunneling of magnetization[1] and quantum phase interference.[2] In 1993, the polynuclear manganese cluster $[Mn_{12}O_{12}(CH_3COO)_{16}(H_2O)_4]\cdot 2\ CH_3COOH\cdot 4\ H_2O$ was reported to be the first single molecule magnet by Sessoli et al.[3] The synthesis of this complex was first reported by T. Lis in 1980.[4] This dodecanuclear manganese cluster was found to have an $S = 10$ ground state and shows magnetization hysteresis below 4 K.[3] Since 1993, many polynuclear transition-metal complexes have been found to show SMM behavior.

A vast majority of SMMs have been synthesized using transition metals such as iron, manganese, and nickel, with

* To whom correspondence should be addressed. E-mail: dhendrickson@ucsd.edu.
† University of California at San Diego.
‡ Quantum Design.
§ University of Central Florida.

(1) (a) Gatteschi, D.; Sessoli, R. *Angew. Chem., Int. Ed.* **2003**, *42*, 3. (b) Christou, G.; Gatteschi, D.; Hendrickson, D. N.; Sessoli, R. *MRS Bull.* **2000**, *25*, 66.
(2) Wernsdorfer, W.; Sessoli, R. *Science* **1999**, *284*, 133.
(3) (a) Sessoli, R.; Tsai, H.-L.; Schake, A. R.; Wang, S.; Vincent, J. B.; Folting, K.; Gatteschi, D.; Christou, G.; Hendrickson, D. N. *J. Am. Chem. Soc.* **1993**, *115*, 1804. (b) Sessoli, R.; Gatteschi, D.; Caneschi, A.; Novak, M. A. *Nature* **1993**, *365*, 141.
(4) Lis, T. *Acta Crystallogr., Sect. B* **1980**, *36*, 2042.

10.1021/ic800277j CCC: $40.75 © 2008 American Chemical Society
Published on Web 06/21/2008

a majority of SMMs consisting of polynuclear manganese complexes. The complex $[Fe_8O_2(OH)_{12}(tacn)_6]Br_8$, where tacn is triazocycolnonane, is one of the most extensively studied iron SMMs and has an $S = 10$ ground state.[5] SMMs of nickel include the tetranuclear nickel cubane complex $[Ni(hmp)(MeOH)Cl]_4$ with an $S = 4$ ground state.[6] The tetranuclear vanadium complex $[V_4O_2(O_2CPh)_7(bpy)_2]ClO_4$, reported in 1998, is one of the few vanadium SMMs that is known.[7] In addition to the homometallic complexes described above, heterometallic complexes that show SMM behavior have also been reported.[8,9] A small number of manganese−lanthanide and iron−lanthanide SMMs also exist, indicating that the synthesis of SMMs is not limited to transition metals.[10–14]

SMMs have been synthesized having many different nuclearities, ranging from dinuclear[15,16] and trinuclear metal complexes[17] to complexes as large as the Mn_{84} wheel[18] and the heterometallic copper−manganese cluster $[Cu_{17}Mn_{28}O_{40}(tea)_{12}(HCO_2)_6(H_2O)_4]\cdot 36H_2O$, which has a $5^1/_2$ ground state.[19] The smallest SMM known to date is a dinuclear heterometallic copper−manganese complex $[MnCuCl(5\text{-}Br\text{-}sap)_2(MeOH)]$.[15] This complex was synthesized using the ligand 5-bromo-2-salicylideneamino-1-propanol and has an $S = {}^5/_2$ ground state.[15]

SMMs have been reported with many different topologies including cubanes, dicubanes, 1D chains, and 2D or 3D networks. One example of this diversity in topologies is the $[Mn_4(hmp)_6Cl_2]_n(ClO_4)_{2n}$[20] complex, which is a 1D chain of $S = 9$ SMMs that are interconnected by bridging chloride ions. Molecular wheels represent an interesting topology seen in polynuclear transition-metal complexes and have become of great interest and fascination to scientists in recent years. It is believed that transition-metal wheel complexes could be used as qubits for quantum computation.[21] A few of the known molecular wheels exhibit SMM behavior. Among these wheel-shaped SMMs is the Ni_{12} wheel, which was synthesized with the ligand 6-chloro-2-hydroxypyridine; it shows magnetization hysteresis below 0.4 K.[22] Ferromagnetic exchange interactions between 12 nickel(II) centers give this single-stranded wheel an $S = 12$ ground state.[22] The wheel-shaped Mn_{84} SMM is comprised of only Mn^{3+} ions, and shows hysteresis below 1.5 K as a result of a $S = 6$ ground state.[18] In contrast to the Ni_{12} wheel,[22] the Mn_{84} wheel is not a single-stranded loop.[18] A vast majority of molecular wheels that have been synthesized have an even number of metal atoms. Odd-numbered molecular wheels are of interest to scientists studying spin frustration. Winpenny et al. [23] reported in 2004 an odd-numbered heterometallic molecular wheel with the formula $[(C_6H_{11})_2NH_2][Cr_8NiF_9(O_2CC(CH_3)_3)_{18}]$.

A variety of ligands have been employed in the synthesis of these polynuclear wheels, including deprotonated triethanolamine ($teaH^{2-}$), *n*-substituted diethanolamines (dea^{2-}), and the tris-hydroxymethyl propane ligand (H_3tmp). Other wheel-shaped manganese SMMs include the $[Mn_{22}]$ wheels,[24] a series of $[Mn_{12}]$ wheels,[25] and the $[Mn_{16}]$ wheel.[26] The $[Mn_{12}]$ and the $[Mn_{16}]$ wheels are the only single-stranded manganese wheels reported to date. The $[Mn_{16}]$ wheel communicated by Murugesu et al.[26] has the formula $[Mn_{16}(O_2CMe)_{16}(teaH)_{12}]\cdot 16MeCN$ and was found to show magnetization hysteresis below 0.8 K with an $S = 10$ ground state.

The $[Mn_{16}O_{16}(OMe)_6(MeOH)_3(H_2O)_3]\cdot 6H_2O$ cluster reported by Murray et al.[27] in 2002, is not a molecular wheel but is an example of a hexadecanuclear manganese cluster that shows SMM behavior. The triethanolamine ligand has been employed in the synthesis of other polynuclear manganese clusters, such as the series of Mn_4 complexes reported by Berry et al.[28] in 2004 and the tetranuclear manganese clusters reported by Wittick et al.[29] in 2006. The heptanuclear manganese cluster reported by Barra et al.[30]in 1998 also incorporates the triethanolamine ligand.

We herein report two structural analogs of the $[Mn_{16}]$ wheel[26] synthesized using acetate, butyrate, and isobutyrate

(5) Wieghardt, K.; Pohl, K.; Jibril, I.; Huttner, G. *Angew. Chem., Int. Ed.* **1984**, *23*, 77.
(6) Yang, E.-C.; Wernsdorfer, W.; Zakharov, L. N.; Karaki, Y.; Yamaguchi, A.; Isidro, R. M.; Lu, G.; Wilson, S. A.; Rheingold, A. L.; Ishimoto, H.; Hendrickson, D. N. *Inorg. Chem.* **2006**, *45*, 529.
(7) Castro, S. L.; Sun, Z.; Grant, C. M.; Bollinger, J. C.; Hendrickson, D. N.; Christou, G. *J. Am. Chem. Soc.* **1998**, *120*, 2365.
(8) Oshio, H.; Nihei, M.; Koizumi, S.; Shiga, T.; Nojiri, H.; Nakano, M.; Shirakawa, N.; Akatsu, M. *J. Am. Chem. Soc.* **2005**, *127*, 4568.
(9) Yoon, J. H.; Lim, J. K.; Kim, H. C.; Hong, C. S. *Inorg. Chem.* **2006**, *45*, 9613.
(10) Murugesu, M.; Mishra, A.; Wernsdorfer, W.; Abboud, K. A.; Christou, G. *Polyhedron* **2006**, *25*, 613.
(11) Mishra, A.; Wernsdorfer, W.; Abboud, K. A.; Christou, G. *J. Am. Chem. Soc.* **2004**, *126*, 15648.
(12) Costes, J. P.; Dahan, F.; Wernsdorfer, W. *Inorg. Chem.* **2006**, *45*, 5.
(13) Ferbinteanu, M.; Kajiwara, T.; Choi, K.-W.; Nojiri, H.; Nakamoto, A.; Kojima, N.; Cimpoesu, F.; Fujimura, Y.; Takaishi, S.; Yamashita, M. *J. Am. Chem. Soc.* **2006**, *128*, 9008.
(14) Kachi-Terajima, C.; Miyasaka, H.; Saitoh, H.; Shirakawa, N.; Yamashita, M.; Clerac, R. *Inorg. Chem.* **2007**, *46*, 5861.
(15) Oshio, H.; Nihei, M.; Yoshida, A.; Nojiri, H.; Nakano, M.; Yamaguchi, A.; Karaki, Y.; Ishimoto, H. *Chem.—Eur. J.* **2005**, *11*, 843.
(16) Miyasaka, H.; Clerac, R.; Wernsdorfer, W.; Lecren, L.; Bonhomme, C.; Sugiura, K.; Yamashita, M. *Angew. Chem., Int. Ed.* **2004**, *43*, 2801.
(17) Scott, R.T. W.; Parsons, S.; Murugesu, M.; Wernsdorfer, W.; Christou, G.; Brechin, E. K. *Chem Comm.* **2005**, 2083.
(18) Tasiopolous, A. J.; Vinslava, A.; Wernsdorfer, W.; Abboud, K. A.; Christou, G. *Angew. Chem., Int. Ed.* **2004**, *43*, 2117.
(19) Wang, W. G.; Zhou, A. J.; Zhang, W. X.; Tong, M. L.; Chen, X. M.; Nakano, M.; Beedle, C. C.; Hendrickson, D. N. *J. Am. Chem. Soc.* **2007**, *129*, 1014.
(20) Yoo, J.; Wernsdorfer, W.; Yang, E.; Nakano, M.; Rheingold, A. L.; Hendrickson, D. N. *Inorg. Chem.* **2005**, *44*, 3377.
(21) Affronte, M.; Casson, I.; Evangilisti, M.; Candini, A.; Carreta, S.; Muryn, C.; Teat, S. J.; Timco, G. A.; Wernsdorfer, W.; Winpenny, R. E. P. *Angew. Chem., Int. Ed.* **2005**, *44*, 6496.
(22) (a) Cadiou, C.; Murrie, M.; Paulsen, C.; Villar, V.; Wernsdorfer, W.; Winpenny, R. E. P. *Chem. Comm.* **2001**, *24*, 2666. (b) Andres, H.; Basler, R.; Blake, A.; Cadiou, C.; Chaboussant, G.; Grant, C.; Gudel, H.; Murrie, M.; Parsons, S.; Paulsen, C.; Semadini, F.; Villar, V.; Wernsdorfer, W.; Winpenny, R. E. P. *Chem.—Eur. J.* **2002**, *8*, 4867.
(23) Cador, O.; Gatteschi, D.; Sessoli, R.; Larsen, F. K.; Overgaard, J.; Barra, A. L.; Teat, S. J.; Timco, G. A.; Winpenny, R. E. P. *Angew. Chem., Int. Ed.* **2004**, *43*, 5196.
(24) Manoli, M.; Prescimone, A.; Bagai, R.; Mishra, A.; Murugesu, M.; Parsons, S.; Wernsdorfer, W.; Christou, G.; Brechin, E. K. *Inorg. Chem.* **2007**, *46*, 6968.
(25) (a) Rumberger, E. M.; Zakharov, L. N.; Rheingold, A. L.; Hendrickson, D. N. *Inorg. Chem.* **2004**, *43*, 6531. (b) Rumberger, E. M.; Shah, S. J.; Beedle, C. C.; Zakharov, L. N.; Rheingold, A. L.; Hendrickson, D. N. *Inorg. Chem.* **2005**, *44*, 2742.
(26) Murugesu, M.; Wernsdorfer, W.; Abboud, K.; Christou, G. *Angew. Chem., Int. Ed.* **2005**, *44*, 892.
(27) (a) Price, D. J.; Batten, S. R.; Moubaraki, B.; Murray, K. S. *Chem. Comm.* **2002**, 762. (b) Price, D. J.; Batten, S. R.; Moubaraki, B.; Murray, K. S. *Polyhedron.* **2007**, *26*, 305.
(28) Wittick, L. M.; Murray, K. S.; Moubaraki, B.; Batten, S. R.; Spiccia, L.; Berry, K. J. *Dalton Trans.* **2004**, 1003.

carboxylate ligands that are different than employed in the one known [Mn_{16}] wheel. These new [Mn_{16}] wheels were synthesized from simple manganese(II) salts using triethanolamine, a tripodal ligand with three alcohol arms.

Experimental Section

Synthesis. All manipulations were performed under aerobic conditions. The chemicals manganese(II) acetate, triethanolamine, and triethylamine were purchased from Sigma-Aldrich and used without further purification. Manganese(II) butyrate and manganese(II) isobutyrate were prepared as described.[31,32]

$[Mn_{16}(CH_3COO)_8(CH_3CH_2CH_2COO)_8(teaH)_{12}]\cdot 10$ MeCN (**1**·10 MeCN). A 25 mL CH_2Cl_2 solution of triethanolamine (0.74 g, 5 mmol) was added to a solution of manganese(II) acetate (0.61 g, 2.5 mmol) and manganese(II) butyrate (0.57 g, 2.5 mmol) in 50 mL CH_2Cl_2. To this solution was added triethylamine (0.69 mL, 5 mmol) and the solution was stirred overnight. The solution was concentrated by vacuum distillation to yield an oil. MeCN (80 mL) were added to this oil. Slow evaporation of the MeCN solution led to the formation of brown crystals after two weeks. The yield was 14%. Anal. Calcd (found) for **1** $C_{142}H_{257}Mn_{16}N_{23}O_{68}$: C, 37.77 (37.42); H, 6.19 (6.47); N, 4.40 (4.39). Selected IR data (KBr): 3500(m, br), 3000(m, br), 1580(s), 1410(m), 1100(m), 900(w), 600(w).

$[Mn_{16}((CH_3)_2CHCOO)_{16}(teaH)_{12}]\cdot 4CHCl_3$ (**2**·4$CHCl_3$). To a solution of manganese(II) isobutyrate (1.14 g, 5 mmol) in 75 mL $CHCl_3$ was added 1 equiv of the ligand triethanolamine (0.74 g, 5 mmol) in 25 mL $CHCl_3$. To this solution was added 1 equiv of triethylamine (0.69 mL, 5 mmol) and the solution was stirred overnight. The solution was then concentrated by vacuum distillation to yield a volume of approximately 30 mL. The solution was then divided equally into two flasks. MeCN (80 mL) was added to each flask. Brown crystals were obtained after two days by slow evaporation of the MeCN solution. The yield was 19%. Anal. Calcd (found) for **2**. $C_{140}H_{272}Cl_{12}Mn_{16}N_{12}O_{68}$: C, 37.26 (37.70); H, 6.03 (6.39); N, 3.72 (4.12). Selected IR data (KBr): 3400(m, br), 3000(m, br), 1580(s), 1400(s), 1100(m), 600(w).

Physical Measurements. Infrared spectra were recorded as KBr discs using a Thermo-Nicolet Avatar series spectrophotometer. All elemental analyses were performed by Numega Resonance Laboratories (San Diego, CA). The DC magnetic susceptibility data were collected on a Quantum Design MPMS magnetometer equipped with a 5 T magnet at the University of California at San Diego. Microcrystalline samples were measured in a gelatin capsule and restrained using eicosane to prevent torquing. Diamagnetic corrections were applied to the magnetic susceptibility data using Pascal's constants. The AC magnetic susceptibility data were collected on a Quantum Design PPMS magnetometer at Quantum Design in San Diego, California. Magnetization hysteresis measurements were carried out on a single crystal using a micro-Hall effect magnetometer[33] at the University of Central Florida.

Table 1. Crystallographic Data and Refinement Parameters for **1**·10 MeCN and **2**·4$CHCl_3$

	1·10MeCN	**2**·4$CHCl_3$
formula	$Mn_{16}C_{140}H_{257}N_{22}O_{68}$	$Mn_{16}C_{140}H_{272}N_{12}O_{68}Cl_{12}$
fw	4215.72	4516.14
T [K]	208(2)	100(2)
λ [Å]	0.71073	0.71073
cryst syst	tetragonal	monoclinic
space group	$I4_1/a$	$C2/c$
a [Å]	33.519(4)	21.473(5)
b [Å]	33.519(4)	26.819(6)
c [Å]	16.659(2)	35.186(7)
α [deg]	90	90
β [deg]	90	93.447(5)
γ [deg]	90	90
V [Å^3]	18716(3)	20227(7)
	4	4
D_{calcd} [mg m^{-3}]	1.511	1.483
abs. coefficient [mm^{-1}]	1.128	1.200
$F(000)$	8868	9376
θ range [deg]	2.19 to 25.03°	2.08 to 25.03°
comp. to θ [25.00°]	99.9%	92.7%
max. and min. transmission	0.9778 and 0.8956	0.9764 and 0.9207
data/restraints/params	8249/2/494	16 594/0/1103
GOF on F^2	0.906	1.116
R(F)[a] [$I > 2\sigma(I)$]	0.0758	0.0925
R(wF^2)[b] [$I > 2\sigma(I)$]	0.1887	0.2436
largest diff. peak and hole [e·Å^{-3}]	0.782 and −0.492	1.182 and −0.555

[a] $R = \Sigma||F_o| - |F_c||/\Sigma|F_o|$. [b] $R(\omega F^2) = \{\Sigma[\omega(F_o^2 - F_c^2)^2]/\Sigma[\omega(F_o^2)^2]\}^{1/2}$; $\omega = 1/[\sigma^2(F_o^2) + (aP)^2 + bP]$, $P = [2F_c^2 + \max(F_o, 0)]/3$.

X-ray Crystallography. Crystals were mounted on a CryoLoop with Paratone-N oil. Diffraction intensity data were collected at 208 K (**1**) and 100 K (**2**) on a Bruker Smart Apex CCD diffractometer with Mo Kα radiation, integrated using Bruker *SAINT* software program, and corrected for absorption using the Bruker *SADABS* program. Crystallographic data and refinement parameters for **1** and **2** are given in Table 1.

1 and **2** were solved by direct methods (*SHELXS-97*), developed by successive difference Fourier syntheses, and refined by full matrix least-squares on all F^2 data. All non-hydrogen atoms were refined as being anisotropic, and hydrogen atoms were placed in calculated positions with temperature factors fixed at 1.2 or 1.5 times the equivalent isotropic U of the C atoms to which they were bonded. Disordered solvate molecules (MeCN for **1** and $CHCl_3$ for **2**) were treated by the Squeeze method, the details of which can be found in the CIF files (Supporting Information). The C5, C6, C15, and C16 of the butyrate ligands in **1** are positionally disordered, yielding larger-than-normal thermal ellipsoids.

Results and Discussion

Crystal Structures. $[Mn_{16}(CH_3COO)_8(CH_2CH_2COO)_8(teaH)_{12}]\cdot 10$ MeCN (**1**·10MeCN). Complex **1** crystallizes in the tetragonal $I4_1/a$ space group, the structure of which is shown in Figure 1. An *ORTEP* of the structure can be found in Figure S1 (Supporting Information). The structure comprises a [Mn_{16}] wheel with a closed sinusoidal or saddle-shaped topology (Mn−O core connectivity shown in Figure 2 and side view shown in Figure 3) analogous to the molecule communicated by Murugesu et al. in 2005.[26] The formula of **1** differs from this previously reported wheel in that half of the bridging acetate ligands have been replaced by *n*-butyrate ligands. The wheel consists of 8 manganese(II) and 8 manganese(III) ions alternating in a single-stranded

(29) Wittick, L. M.; Jones, L. F.; Jensen, P.; Moubaraki, B.; Spiccia, L.; Berry, K. J.; Murray, K. S. *Dalton Trans.* **2006**, 1534.
(30) Pilawa, B.; Kelemen, M. T.; Wanka, S.; Geisselmann, A.; Barra, A. L. *Europhys. Lett.* **1998**, *43*, 7.
(31) Baca, S. G.; Sevryugina, Y.; Clerac, R.; Malaestean, I.; Gerbeleu, N.; Petrukhina, M. A. *Inorg. Chem. Commun.* 2005, *8*, 474.
(32) Synthesis of $Mn(CH_3CH_2CH_2COO)_2$: To a slurry of manganese(II) carbonate (0.3 g, 0.27 mol) in 200 mL water is added 30 mL of butyric acid. After allowing the solution to stir for a few days, the solution is filtered and the filtrate is evaporated in vacuo to yield pale-pink crystals. The yield was 28%. Anal. Calcd (found) for $C_8H_{14}O_4Mn$: C, 41.9 (40.7); H, 6.15 (6.31).
(33) Kent, A. D.; von Molnar, S.; Gider, S.; Awschalom, D. D. *J. Appl. Phys.* **1994**, *76*, 6656.

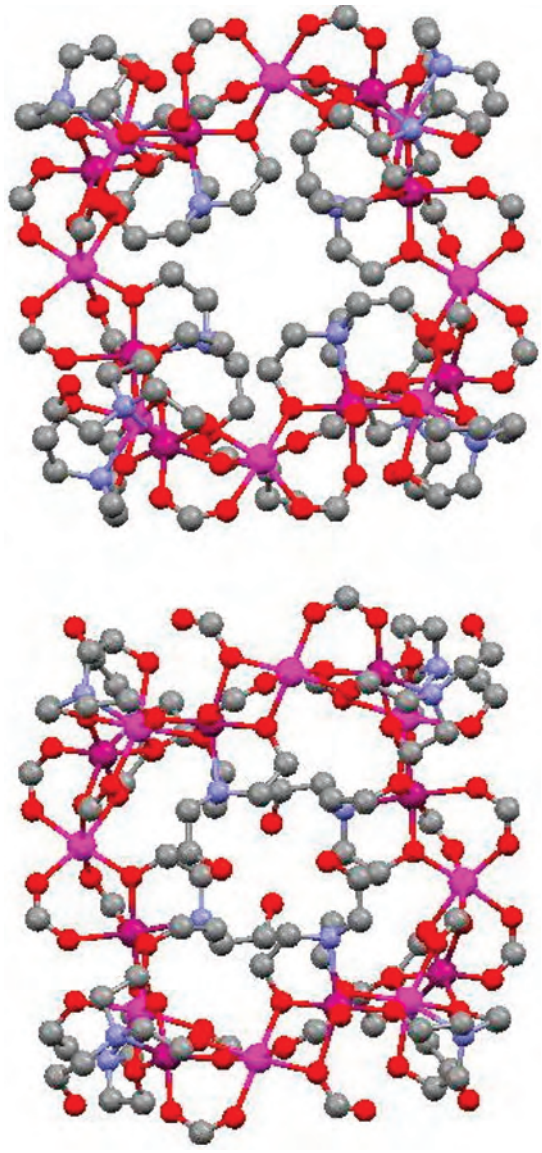

Figure 1. **1** (top) and **2** (bottom) with manganese(II), pink; manganese(III), purple; carbon, gray; oxygen, red; nitrogen, blue. Aliphatic groups on carboxylates are omitted for clarity.

arrangement. The valency of the manganese ions was determined by bond valence sum analyses as well as the presence of Jahn−Teller (JT) distortion around the manganese(III) ions. Selected Jahn−Teller distorted bond distances and angles for **1** can be found in Table S1 (Supporting Information). The orientation of the Jahn−Teller axes can also be seen in Figure 3.

Each manganese(III) ion in **1** possesses a six-coordinate, distorted octahedral geometry with average JT elongated manganese(III)−O bonds of 2.25 Å and manganese(III)−N bonds of 2.38 Å. The manganese(III) ions are chelated by a monoprotonated $teaH^{2-}$ ligand in a tridentate fashion with the protonated alcohol arm remaining uncoordinated. The two alkoxide oxygen atoms bound to the manganese(III) ions also bridge the adjacent manganese(II) ions. Four of the uncoordinated alcohol arms are situated on the periphery of the wheel while the other six are located on the interior of the wheel. The four remaining $teaH^{2-}$ ligands are bound to every other manganese(II) ion in a tetradentate chelate mode where all three alcohol arms, including the protonated arm, are coordinated to the metal. This binding mode leads to seven-coordinate, distorted pentagonal-bipyramidal geometry around these four manganese(II) ions, whereas the other four manganese(II) ions are six-coordinate.

The acetate ligands form a η^1, η^1, μ^2 bridge between each seven-coordinate manganese(II) and an adjacent manganese(III) ion. The *n*-butyrate ligands, however, bind in two different modes. Four of the *n*-butyrates bridge the six-coordinate manganese(II) and manganese(III) ions in a similar μ^2 binding mode as the acetate groups. The four remaining butyrates bind in a less common η^1, η^2, μ^3 bridging mode, linking the manganese(III), six-coordinate manganese(II), and seven-coordinate manganese(II) ions. Analogous bonding was also seen in the previously reported $[Mn_{16}]$ wheel.[26]

1 exhibits both intra- and intermolecular hydrogen bonding interactions (Figures S2 and S3 respectively, Supporting Information). The protonated alcohol arm of the $teaH^{2-}$ ligand that is bound to the seven-coordinate manganese(II) ion interacts with a neighboring oxygen atom of a bridging acetate ligand. The unbound alcohol arms on the interior of the wheel form H-bonding contacts with bridging alkoxide oxygen atoms. The free alcohol arms on the outside of the wheel are involved in intermolecular H-bonding with acetate and *n*-butyrate oxygen atoms on adjacent wheels. This extensive H-bonding network allows for the oddly shaped wheels to pack in a rather efficient and compact manner.

The unit cell of **1** contains four molecules as shown in Figure S4 (Supporting Information). Along the *a* axis, the wheels are seen from the side-on perspective and stack in an alternating up and down pattern-forming channels. The *c* axis provides a top view of the wheels that shows how the easy axes of each molecule (through the center of the wheel) are aligned parallel to one another along the *c* direction. The unit cell also contains 10 disordered acetonitrile solvate molecules per wheel, which occupy an average void whose centroid is located ∼27 Å from the center of the wheel.

$[Mn_{16}((CH_3)_2CHCOO)_{16}(teaH)_{12}]\cdot 4CHCl_3$ (**2**·$4CHCl_3$). Figure 1 shows the structure of **2**, which crystallizes in the monoclinic *C*2/*c* space group. (An ORTEP can be found in Figure S1 (Supporting Information).) The asymmetric unit consists of one-half of the target molecule with the symmetry-equivalent positions generated by the $-x, y, {}^1/_2 - z$ transformation. **2** exhibits the same $[Mn_{16}]$ core as seen in the structure of **1** (Figures 2 and 3); however, all of the carboxylate positions are occupied by isobutyrate ligands. Selected Jahn−Teller distorted bond distances and angles are given for **2** in Table S2 (Supporting Information).

The crystal structure of **2** is similar to **1** in that it contains 8 manganese(II) (four seven-coordinate and four six-coordinate) and 8 manganese(III) ions in an alternating arrangement. The average JT elongation bond lengths are 2.22 Å for Mn(III)−O and 2.38 Å for Mn(III)−N. All of the monoprotonated $teaH^{2-}$ ligands exhibit the same binding modes as in **1** (both tridentate and tetradentate). The isobutyrates occupy similar positions as the acetate and *n*-butyrate ligands in **1** but differ slightly in their bridging

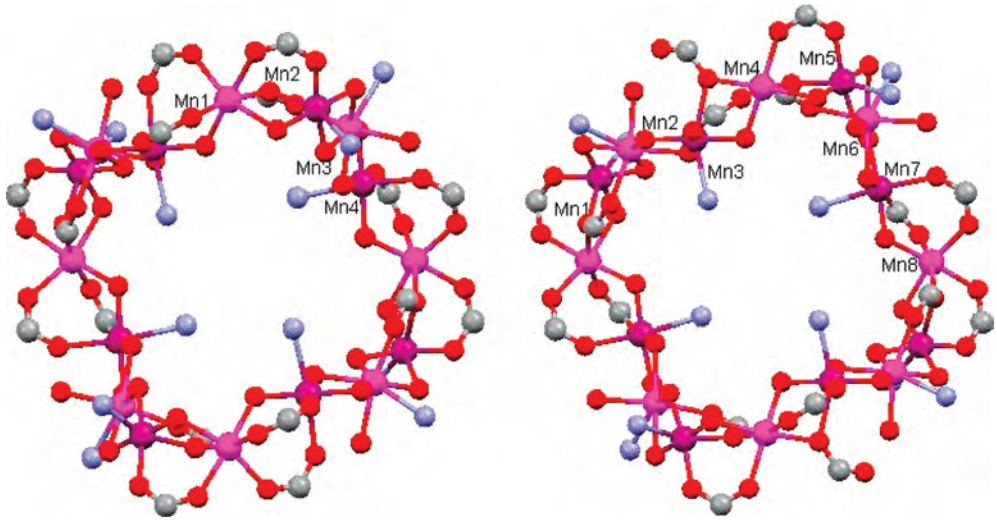

Figure 2. Core connectivity for **1** (left) and **2** (right) with the same color scheme as Figure 1.

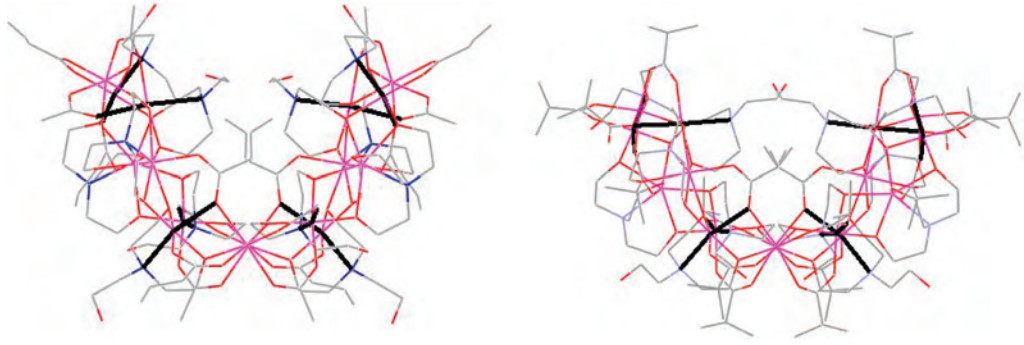

Figure 3. Side-views of **1** (left) and **2** (right) with Jahn−Teller axes in bold.

modes. Whereas 10 of the isobutyrates bind in the η^1, η^1, μ^2 mode and four bind in the η^1, η^2, μ^3 mode as observed in **1**, the remaining two isobutyrates bind in the less common η^0, η^2, μ^2 bridging mode where two adjacent six-coordinate manganese atoms are bridged through a single oxygen atom of the isobutyrate ligand.

2 also exhibits extensive H-bonding networks similar to that of **1** (Figures S2 and S3 in the Supporting Information). The protonated alcohol arm of the $teaH^{2-}$ ligand bound to a manganese(II) ion is within H-bonding distance to either the alkoxide oxygen atom of a neighboring η^1, η^1, μ^2-isobutyrate ligand or the uncoordinated oxygen atom of the η^0, η^2, μ^2-isobutyrate. Two of the free alcohol arms on the interior of the wheel form a weak H-bonding contact across the wheel that is not observed in **1**. The outer edge of the wheel contains four uncoordinated alcohol arms which form an intermolecular H-bonding network through unbound alcohol arms on adjacent wheels.

Though the shape and H-bonding pathways of **1** and **2** are similar, the crystal packing of each unit cell is slightly different. The unit cell of **2** also contains four molecules as shown in Figure S5 in the Supporting Information. As seen in the unit cell of **1**, the wheels in **2** also stack from the side-on view along the *a* axis. However, the wheels in each individual channel are aligned in the same direction (not alternating as in **1**). The easy axes of the wheels in **2** are oriented along the *b* axis in this case and the wheels are layered in staggered, overlapping sheets. **2** also contains four chloroform solvate molecules per wheel, only one of which was ordered enough to be modeled in the crystal structure. The refined chloroform molecules (four per unit cell) occupy the solvent voids between adjacent molecules and exhibit weak H-bonding to the uncoordinated alcohol arms of the $[Mn_{16}]$ wheels.

Direct Current Magnetic Susceptibility Studies. dc magnetic susceptibility data were collected on microcrystalline samples of **1** and **2** in a temperature range of 1.8−300 K in a 1 T applied magnetic field. The 1 T dc magnetic susceptibility data for **1** are shown in Figure S6 in the Supporting Information. The product of the molar magnetic susceptibility and the absolute temperature ($\chi_M T$) at 300 K is 53.1 $cm^3 \cdot K \cdot mol^{-1}$ and gradually decreases with temperature until a value of 41.7 $cm^3 \cdot K \cdot mol^{-1}$ is reached at 25 K. A further decrease in the temperature to 10 K leads to an increase in the $\chi_M T$ value, which is followed by an abrupt decrease below 10 K until a value of 19 $cm^3 \cdot K \cdot mol^{-1}$ is reached at 1.8 K.

The DC magnetic susceptibility data for complex **2** are shown in Figure S7 in the Supporting Information (plotted as $\chi_M T$ vs T) starting at 300 K with a value of 55.6 $cm^3 \cdot K \cdot mol^{-1}$. As the temperature is decreased, this value is found to remain more or less constant in the 300−80 K range. There is a slight decrease in the $\chi_M T$ in the temperature range between 80 and 25 K, below which the

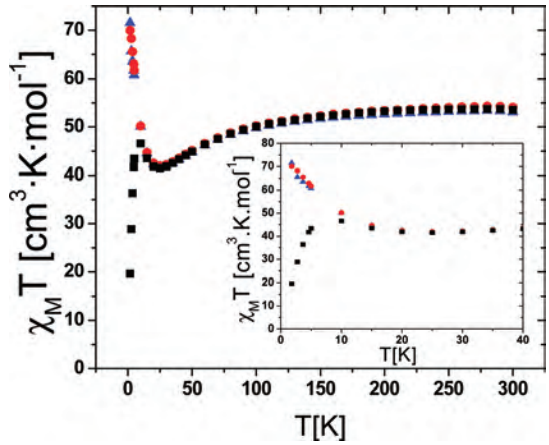

Figure 4. Field dependence of $[Mn_{16}(CH_3COO)_8(CH_3CH_2CH_2COO)_8(teaH)_{12}]\cdot 10$ MeCN (**1**·10 MeCN). Data were collected with applied fields of 1 T (■), 0.1 T (●), and 0.01 T (▲) in a temperature range of 1.8−300 K.

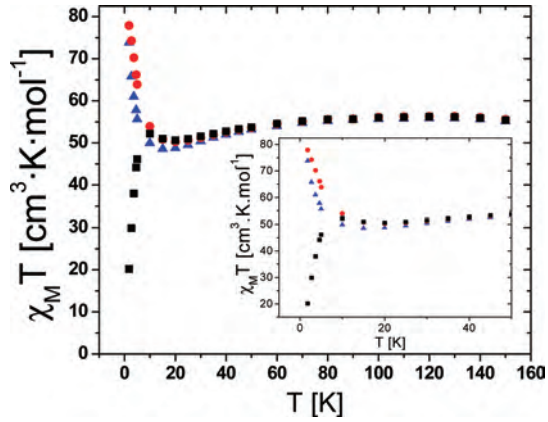

Figure 5. Field dependence of $[Mn_{16}((CH_3)_2CHCOO)_{16}(teaH)_{12}]\cdot 4\ CHCl_3$ (**2**·4 $CHCl_3$). Data were collected with applied fields of 1 T (■), 0.1 T (●), and 0.01 T (▲) in a temperature range of 1.8−150 K.

$\chi_M T$ value increases until a temperature of approximately 10 K is reached. Below 10 K, there is an abrupt drop in the magnetic susceptibility until a value of 22 $cm^3\cdot K\cdot mol^{-1}$ is reached at 1.8 K. For **1** and **2**, the value of $\chi_M T$ at 300 K is found to be lower than the spin-only value of 59 $cm^3\cdot K\cdot mol^{-1}$ expected for noninteracting 8 manganese(II) and 8 manganese(III) ions.

The dc magnetic susceptibility data were also collected at fields of 0.1 and 0.01 T, in addition to the 1 T data for **1** and **2**. Plots of the low field data are shown in Figure 4 for **1** and in Figure 5 for **2**. At temperatures lower than 15 K, there is a magnetic field dependence observed. The data collected at 1 T for both complexes show an increase in the $\chi_M T$ value as the temperature is decreased from 25 to10 K, below which there is an abrupt decrease in the magnetic susceptibility. At the lower fields of 0.1 and 0.01 T, however, the $\chi_M T$ value continues to increase as the temperature is decreased from 25 K down to 1.8 K. There is no decrease in the magnetic susceptibility below 10 K as seen in the 1 T data. This observed field dependence of the $\chi_M T$ versus T data for **1** and **2** can be explained by considering the effect of the Zeeman interaction as the field is varied from 0.01−1 T.

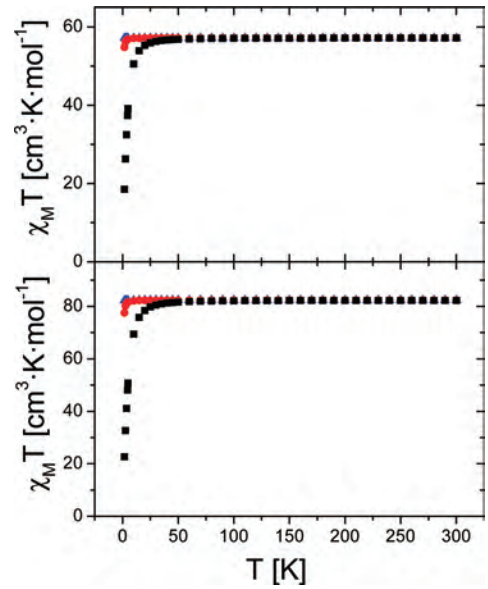

Figure 6. Top plot shows field dependence plot for calculated $\chi_M T$ vs T data expected for a spin-only ($g = 2$) complex with a $S = 10$ ground state. Bottom plot shows the field dependence plot for calculated $\chi_M T$ vs T data expected for a spin-only ($g = 2$) complex with an $S = 12$ ground state. Data are calculated for applied magnetic fields of 0.01 T (▲), 0.1 T (●), and 1 T (■).

As will be shown below, the spins of the ground state for **1** and **2** are in the range of $S = 10$ and $S = 12$. We have calculated $\chi_M T$ versus T data expected for a spin-only ($g = 2$) complex with either a $S = 10$ or a $S = 12$ ground state in an external magnetic field of 0.01, 0.1, or 1 T (Figure 6). As can be seen, the $\chi_M T$ versus T plot is essentially temperature independent down to 1.8 K when the field is either 0.01 or 0.1 T. Thus, the Zeeman interaction is quite small at these field values compared to kT at 1.8 K. On the other hand, it can be seen that both of these spin-only cases ($S = 10$ or 12) exhibit a temperature dependence, exhibiting a pronounced decrease in $\chi_M T$ below 25 K. The experimental $\chi_M T$ versus T plots for **1** and **2** (Figures 4 and 5) can be explained as follows. In the 0.01 and 0.1 T cases there are several states with different spins thermally populated in the 300−50 K range. Only when the temperature is decreased below 25 K do we see an increase in $\chi_M T$ due to the fact that only the $S = 10$ or 12 ground states are thermally populated. When the external field is 1 T, then the increase in $\chi_M T$ as the temperature is decreased below 25 K is offset be the Zeeman interaction, and the net result is that $\chi_M T$ decreases rapidly as the temperature is decreased.

To determine the spin of ground-state for both complexes and the magnitude of zero-field splitting, variable field magnetization data were collected at different fields at temperatures in the range of 1.8 K- 4.0 K. Ground crystalline samples of complexes **1** and **2** were embedded in eicosane to prevent torquing of the magnetically anisotropic particles and subjected to fields of 0.1 to 5.0 T. Plots of reduced magnetization, $M/N\beta$ (where N is Avogadro's number and B is the nuclear Bohr magneton) versus H/T are shown in Figures 7 and 8 for complex **1** and Figures S8 and S9 for complex **2**. Since the $\chi_M T$ vs T data above indicate that there are low-lying excited spin states, the $M/N\beta$ vs H/T data were

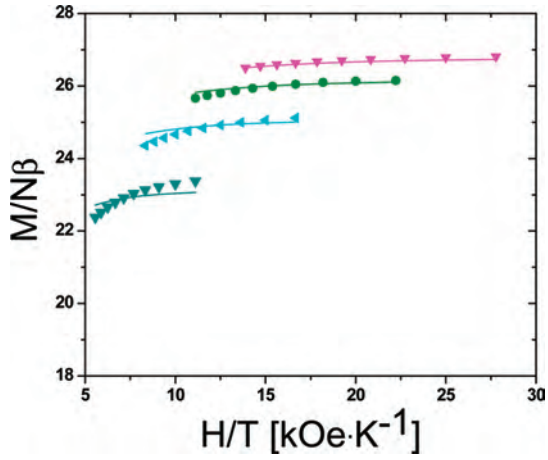

Figure 7. Plot of the reduced magnetization ($M/N\beta$) vs H/T, where M is the molar magnetization, N is Avogadro's number and β is the Bohr magneton, H is the applied magnetic field in kOe, and T is the temperature in K for $[Mn_{16}(CH_3COO)_8(CH_3CH_2CH_2COO)_8(teaH)_{12}]\cdot 10MeCN$ (**1**·10MeCN). Data were collected at 5T (right solid triangle), 4T (●), 3T (left solid triangle), 2T (▼) in the temperature range of 1.8−4 K. Solid lines represent the least-squares fit of the data.

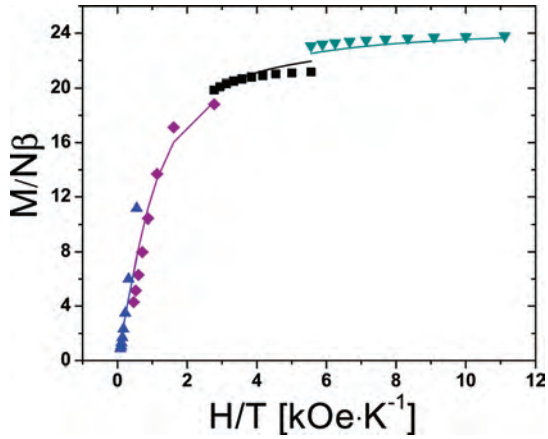

Figure 8. Plot of the reduced magnetization ($M/N\beta$) vs H/T, where M is the molar magnetization, N is Avogadro's number and β is the Bohr magneton, H is the applied magnetic field in kOe, and T is the temperature in K for $[Mn_{16}(CH_3COO)_8(CH_3CH_2CH_2COO)_8(teaH)_{12}]\cdot 10MeCN$ (**1**·10MeCN). Data were collected at 2T (▼), 1T (■), 0.5T (♦), 0.1T (▲) in a temperature range of 1.8−10 K. Solid lines represent least-squares fit of the data.

fit in two different field ranges, one running from 2 to 5 T and the other in the 0.1 to 2 T range. If there is an excited spin state with a spin that is larger than the ground state, then the fit of the data in the higher field range would be different than for fitting the low-field data. It was assumed in all cases that only one spin state is thermally populated and that the spin Hamiltonian given in eqn. 1 is appropriate,

$$\hat{H} = D\hat{S}_Z^2 + E(\hat{S}_X^2 - \hat{S}_Y^2) + \mu_0 g \mu_B \hat{S}\cdot\hat{B} \qquad (1)$$

where D is the axial zero-field splitting (ZFS) parameter, E is the rhombic ZFS parameter, and $\mu_0 B$ is the applied field. The third term in eq 1 is for the Zeeman interaction. The full Hamiltonian matrix (2S×2S) was diagonalized for each setting of the parameters g, D, and E. The resulting eigenvalues, E_i, and their dependency on the magnetic field, $\delta E_i/\delta H$, were used to calculate the magnetization according to eq 2.

$$M = N\sum_i(\delta E_i/\delta H)\exp(-E_i/kT)/\sum_i \exp(-E_i/kT) \qquad (2)$$

A powder average was calculated for each setting of the parameters. The high-field reduced magnetization data for **1** were fit with the parameters $S = 13$, $g = 2.1$, $D = -0.13$ cm^{-1}, and $E = -0.05$ cm^{-1}, as shown in Figure 7. The data collected at much lower fields (shown in Figure 8) were fit with the parameters $S = 13$, $g = 1.8$, and $D = -0.03$ cm^{-1}. For **2**, the fits for the high-field reduced magnetization data collected at different fields ranging from 2 to 5 T are shown in Figure S8 in the Supporting Information. The data were fit with the parameters $S = 14$, $g = 2$, $D = -0.08$ cm^{-1}, and $E = -0.03$ cm^{-1}. The data collected at lower fields ranging from 0.1−2 T (shown in Figure S9 in the Supporting Information) indicate an $S = 13$ ground state, with $g = 1.9$, $D = -0.84$ cm^{-1}, and $E = 0.0$ cm^{-1} for **2**.

The fits of the high-field and low-field reduced magnetization data indicate that complexes **1** and **2** have large-spin ground states. A higher value is obtained for the spin ground state from the fits of the high-field reduced magnetization data compared to the fits of the low-field reduced magnetization data for **2**. This is due to the population of low-lying excited states at higher fields. A further determination of the spin of the ground state was carried out by the extrapolation of the in-phase ac susceptibility data.

Alternating Current Magnetic Susceptibility Studies. ac magnetic susceptibility data were collected on **1** and **2** in a 0.06 Oe applied dc field, with an oscillating ac field of 0.99 Oe. The top portions of Figures 9 and 10 show plots of the in-phase molar ac susceptibility ($\chi'_M T$) versus temperature, whereas the bottom portions show plots of the out-of-phase molar ac susceptibility (χ''_M) versus temperature. Data were collected at six different frequencies, ranging from 50 to 10 000 Hz and at temperatures in the 1.8−5 K range.

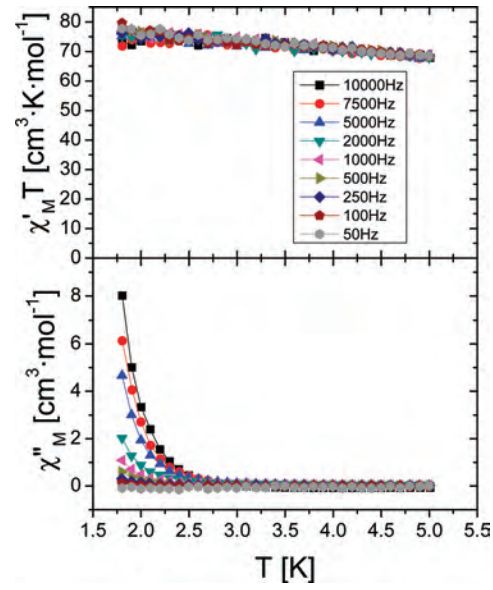

Figure 9. The upper plot shows the χ'_M versus temperature, where $\chi'_M T$ is the molar in-phase ac susceptibility for $[Mn_{16}(CH_3COO)_8(CH_3CH_2CH_2COO)_8(teaH)_{12}]\cdot 10MeCN$ (**1**·10 MeCN). The lower plot shows the χ''_M versus temperature, where χ''_M is the molar out-of-phase ac susceptibility. The data were collected in a 0.99 Oe oscillating magnetic field and at frequencies ranging from 50 Hz to 10 000 Hz.

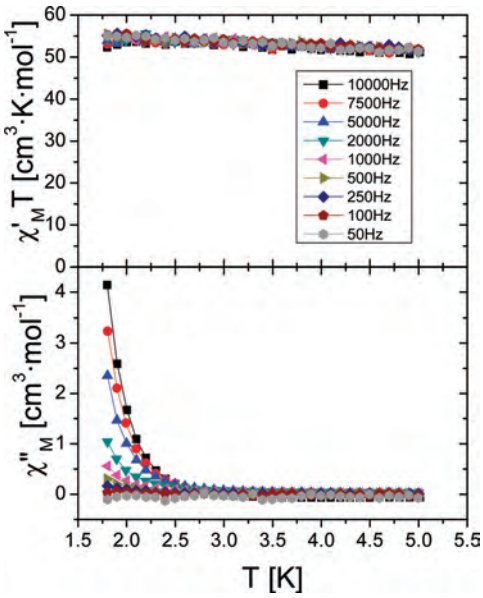

Figure 10. Upper plot shows the $\chi'_M T$ vs temperature, where χ'_M is the molar in-phase ACac susceptibility for $[Mn_{16}((CH_3)_2CHCOO)_{16}(teaH)_{12}]\cdot 4CHCl_3$ (**2**·4CHCl$_3$). The lower plot is χ''_M vs temperature, where χ''_M is the molar out-of-phase ac susceptibility. Data were collected in a 0.99 Oe oscillating magnetic field and were collected at frequencies ranging from 50 Hz to 10 000 Hz.

The ac data for **1** are shown in Figure 9. The value of $\chi'_M T$ is found to be 68.5 cm^3·K·mol^{-1} at 5 K and gradually increases with decreasing temperature until a maximum of 77.7 cm^3· K· mol^{-1} is reached at 1.8 K for the data collected at a frequency of 50 Hz. Data collected at other frequencies also shows a similar trend in that the $\chi'_M T$ value increases with decreasing temperature. **1** shows a frequency-dependent out-of-phase signal in the ac susceptibility below 2.5 K. The ac susceptibility data for **2** are shown in Figure 10. The value of $\chi'_M T$ is 51.3 cm^3·K·mol^{-1} at 5 K and gradually increases with decreasing temperature until a maximum of 55 cm^3·K·mol^{-1} is reached at 1.8 K for the data collected at a frequency of 50 Hz. Data collected at other frequencies shows a similar trend of increase in the $\chi'_M T$ value as the temperature is decreased. **2** also exhibits a frequency-dependent out-of-phase signal in the ac susceptibility below 2.5 K. The presence of a frequency-dependent out-of-phase signal in the ac susceptibility at low temperatures for **1** and **2** is indicative of slow magnetization relaxation relative to the frequency of the oscillating ac field.

To determine the spins of the ground states of **1** and **2**, the in-phase ac susceptibility data were extrapolated to 0 K. The values obtained from the extrapolation can be compared to the values calculated using the spin-only formula. The ac susceptibility data collected at a frequency of 50 Hz were extrapolated to 0 K to give a value of 82 cm^3·K·mol^{-1}, which corresponds to an $S = 12$ ground state for **1**, as shown in Figure 11. A similar type of analysis was carried out on the ac susceptibility data for **2** and is also shown in Figure 11. Extrapolation of the in-phase ac susceptibility data collected at 50 Hz to 0 K gives a value of 62 cm^3·K·mol^{-1}, corresponding to an $S = 11$ ground state for **2**.

A full peak in the out-of-phase signal can not be seen in the temperature range that the measurement was carried out.

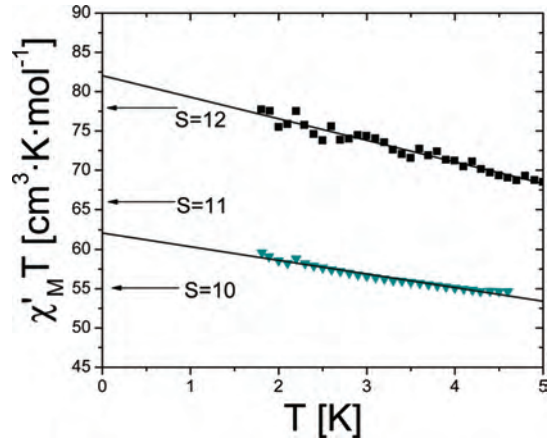

Figure 11. Figure shows extrapolation of in-phase ac susceptibility data to 0 K collected at a frequency of 50 Hz in an oscillating magnetic field of 0.99 Oe for $[Mn_{16}(CH_3COO)_8(CH_3CH_2CH_2COO)_8(teaH)_{12}]\cdot 10MeCN$ (**1**·10 MeCN) (■) and $[Mn_{16}((CH_3)_2CHCOO)_{16}(teaH)_{12}]\cdot 4CHCl_3$ (**2**·4 CHCl$_3$) (left solid triangle).

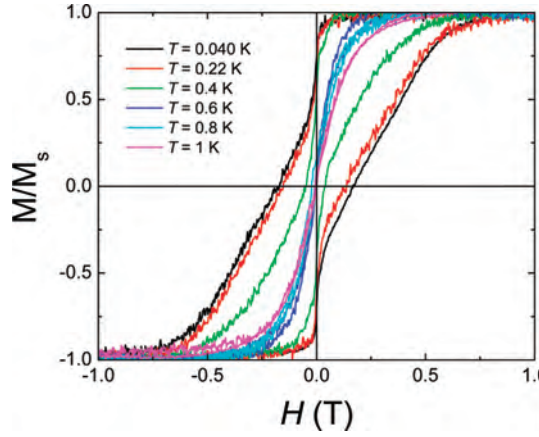

Figure 12. Magnetization Hysteresis plot for $[Mn_{16}((CH_3)_2CHCOO)_{16}(teaH)_{12}]\cdot 4CHCl_3$ (**2**·4 CHCl$_3$). Measurements were carried out in the temperature range of 0.04 to 1 K at a sweep rate of 0.2 T/min.

However, the presence of a frequency dependent out-of-phase signal for **1** and **2** indicates that both complexes are SMMs.

Magnetization Hysteresis Studies. Magnetization hysteresis measurements were carried out on a single crystal of **2**·4CHCl$_3$ in the temperature range of 0.04 to 1 K, at a sweep rate of 0.2 T/ min. Hysteresis data are shown in Figure 12. **2** is found to show magnetization hysteresis at low temperatures. From the hysteresis measurements, the blocking temperature of **2** was determined to be 0.6 K. The blocking temperature is the temperature below which the magnetization is blocked for reversal in the direction and hysteresis is seen. A step is observed at $H = 0$ which is characteristic of quantum tunneling of magnetization (QTM). However, there are no other steps present in the hysteresis loop of **2**.

The absence of steps in a hysteresis loop is common for large SMMs, which are more susceptible to step-broadening effects. Such effects arise from the presence of low-lying excited states as well as a greater distribution of molecular environments. Even the smallest changes in local environments can have significant effects on the magnetic properties of SMMs. The numerous chelating ligands and solvate molecules in these larger complexes often impart disorder in the crystal structure, which leads to this distribution of

environments. Other SMMs that demonstrate this behavior include the $[Mn_{22}]$[24] wheel as well as several other manganese clusters.[34] The $[Mn_{84}]$ wheel also shows this step-broadening effect (no steps are seen), which is thought to be due to the large number of disordered solvate molecules located in the interior of the wheel.[18] It is important to note that none of these SMMs show any steps indicative of QTM in their hysteresis loops including the $H = 0$ step.

The $[Mn_{16}]$ wheel, previously reported by Murugesu et al.,[26] also shows magnetization hysteresis at temperatures below 0.8 K. As expected, the hysteresis loops collected on this SMM are absent of any steps including the step at $H = 0$. This step, however, can clearly be seen in the hysteresis loop of **2** (Figure 12), despite its large size and solvent disorder. Both of these wheels are similar in structure, as discussed in the crystallography section, and cocrystallize with solvate molecules. However, **2** has only 4 $CHCl_3$ (3 disordered, 1 refined) solvate molecules per wheel as opposed to the 16 disordered MeCN reported for the other $[Mn_{16}]$ wheel.[26] The more ordered solvate molecules in **2** reduce the number of microenvironments and allow for the observation of the $H = 0$ step, indicative of magnetization tunneling and thus further confirms that **2** is a single-molecule magnet.

Magnetization hysteresis data were not obtained for **1** due to the nature of the crystals. The crystals of **1** are very thin irregular plates that desolvate quickly, making face indexing very difficult and unreliable. Without face indexing, correct alignment of the wheels in a magnetic field is nearly impossible. The rapid loss of solvate molecules will also lead to a broad range of microenvironments.

Summary and Conclusions

Taking into consideration the fitting of the reduced magnetization data as well as the extrapolation of the ac data to 0 K, the $[Mn_{16}]$ wheel complexes **1** and **2** were determined to have spin ground states of $S = 12$ and 11, respectively. A mixing of low-lying excited states is common in the presence of large dc fields due to the crossing of the M_s levels of low-lying excited states with the M_s levels of the ground-state at high fields, often leading to an incorrect determination of the spin ground-state from reduced magnetization data taken at high fields. The ac data collected in a zero applied dc field is a more-accurate indicator of the spin ground state. Interestingly, $S = 12$ is the highest reported spin ground state for a single-stranded manganese wheel since the wheel complex, $[Mn_{16}O_2(OCH_3)_{12}(tmp)_8(CH_3COO)_{10}]\cdot 3Et_2O$ ($S = 14$), is not a single-stranded wheel.[35]

1 also shows a frequency-dependent out-of-phase signal in the ac susceptibility and is likely to be an SMM that is structurally similar to the $[Mn_{16}(O_2CMe)_{16}(teaH)_{12}]\cdot 16$ MeCN[26] wheel complex. **2** also shows a frequency dependent out-of-phase signal in the ac susceptibility as well as magnetization hysteresis, confirming that this complex is an SMM. The hysteresis loop of **2** shows a distinct step at $H = 0$, indicative of quantum tunneling of magnetization. This step is not normally observed in SMMs of this size due to a large number of microenvironments as a result of several solvate molecules.

2 has some significant structural differences compared to **1** and the previously published $[Mn_{16}]$ wheel ($S = 10$).[26] The crystal structure of **2** indicates that two of the isobutyrate ligands bind in a rare η^0, η^2, μ^2 bridging mode, which facilitates an intermolecular contact between the unbound oxygen atom and a free alcohol arm of an adjacent wheel. **2** also shows a weak intramolecular H-bonding network through the free-alcohol arms of the triethanolamine ligands in the interior of the wheel. This was not observed for **1** or in the previously reported $[Mn_{16}]$ wheel.[26] The structural differences in **2** compared to the other $[Mn_{16}]$ wheels, as well as the partially ordered solvate molecules in the crystal lattice, help rationalize the different spin ground-state, and unprecedented hysteresis measurements.

In conclusion, the family of single-stranded manganese wheel-shaped SMMs has been expanded to three complexes with the addition of the two new complexes, $[Mn_{16}(CH_3COO)_8(CH_3CH_2CH_2COO)_8(teaH)_{12}]\cdot 10$ MeCN (**1**·10MeCN) and $[Mn_{16}((CH_3)_2CHCOO)_{16}(teaH)_{12}]\cdot 4CHCl_3$ (**2**·4$CHCl_3$). The use of triethanolamine with manganese(II) salts has proven to be a useful synthetic route in the preparation of hexadecanuclear manganese wheels. **1** and **2** exhibit magnetic properties that are characteristic of SMMs, in particular a high-spin ground-state and an out-of-phase signal in the ac susceptibility, and **2** shows magnetization hysteresis.

Acknowledgment. This work was supported by the National Science Foundation (NSF).

Supporting Information Available: CCDC nos. 661128 and 661129 that detail the crystallographic information are available from the Cambridge Crystallographic Data center via the Internet at www.ccdc.cam.ac.uk. X-ray crystallographic files in CIF format, figures, and selected interatomic distances and angles for **1** and **2** as well as supporting magnetic data. This material is available free of charge via the Internet at http://pubs.acs.org.

IC800277J

(34) (a) Soler, M.; Rumberger, E.; Folting, K.; Hendrickson, D. N.; Christou, G. *Polyhedron.* **2001**, *20*, 1365. (b) Soler, M.; Wernsdorfer, W.; Folting, K.; Pink, M.; Christou, G. J. *Am. Chem. Soc.* **2004**, *126*, 2156. (c) Sanudo, E. C.; Brechin, E. K.; Boskovic, C.; Wernsdorfer, W.; Yoo, J.; Yamaguchi, A.; Concolino, T. R.; Abboud, K. A.; Rheingold, A. L.; Ishimoto, H.; Hendrickson, D. N.; Christou, G. *Polyhedron.* **2003**, *23*, 2267. (d) Jones, L. F.; Brechin, E. K.; Collison, D.; Harrison, A.; Teat, S. J.; Wernsdorfer, W. *Chem. Commun.* **2002**, 2974.

(35) Manoli, M.; Prescimone, A.; Mishra, A.; Parsons, S.; Christou, G.; Brechin, E. K. *Dalton Trans.* **2007**, *5*, 532.